

2D-Mn₂C₁₂: An Optimal Electrocatalyst with Nonbonding Multiple Single Centers for CO₂-to-CH₄ Conversion

Yaowei Xiang, Wengeng Chen, Meijie Wang, Zi-Zhong Zhu, Shunqing Wu, and Xinrui Cao*



Cite This: *ACS Appl. Mater. Interfaces* 2024, 16, 23199–23208



Read Online

ACCESS |



Metrics & More



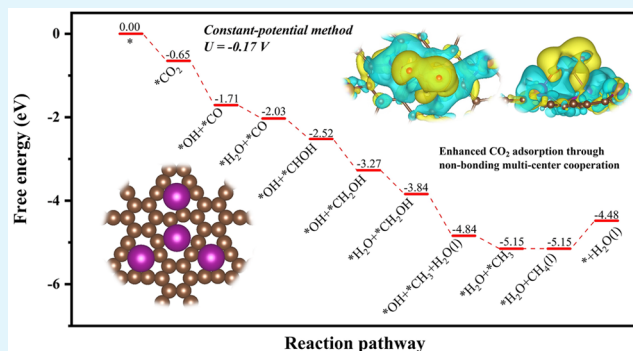
Article Recommendations



Supporting Information

ABSTRACT: The CO₂ reduction reaction (CO₂RR) is a promising method that can both mitigate the greenhouse effect and generate valuable chemicals. The 2D-M₂C₁₂ with high-density transition metal single atoms is a potential catalyst for various catalytic reactions. Using an effective strategy, we screened 1s-Mn₂C₁₂ as the most promising electrocatalyst for the CO₂RR in the newly reported 2D-M₂C₁₂ family. A low applied potential of −0.17 V was reported for the CO₂-to-CH₄ conversion. The relative weak adsorption of H atom and H₂O in the potential range of −0.2 to −0.8 V, ensures the preferential adsorption of CO₂ and the following production of CH₄. The different loading amounts of Mn atoms on γ -graphyne (GY) were also investigated. The Mn atoms prefer doping in the nonadjacent triangular pores instead of the adjacent ones due to the repulsive forces between d-orbitals when the Mn loading is less than 32.3 wt % (5Mn). As the Mn concentration further increases, adjacent Mn atoms begin to appear, and the Mn@GY becomes metallic or half-metallic. The presence of four adjacent Mn atoms increases the d-band center of Mn@GY, particularly the d_{z²} center involved in CO₂ adsorption, thereby enhancing the adsorption capacity for CO₂. These findings indicate that 1s-Mn₂C₁₂ with high Mn atomic loadings is an excellent CO₂RR electrocatalyst, and it provides new insights for designing efficient CO₂RR electrocatalyst.

KEYWORDS: two-dimensional metal–carbon material, multiple single centers, CO₂RR, DFT, constant potential method



1. INTRODUCTION

The graphyne family consists of sp- and sp²-hybridized carbon atoms and is one of the carbon allotropes of graphene. According to numbers of ethyne units between two adjacent benzene ring, the graphyne family is divided into γ -graphyne (GY), graphdiyne (GDY), graphtriyne (GTY), and so on.^{1–3} The successfully synthesized graphdiyne (GDY) aroused people's research interest in the fields of energy conversion, batteries, electronics and catalysis.^{4,5} In recent years, GY has been also experimentally prepared through mechanochemical synthesis⁶ and Sonogashira coupling.⁷ GY and GDY are both semiconductor materials with low intrinsic catalytic activity.^{3,8–12} Their large specific surface area and uniformly distributed triangular pores make them good catalyst carriers for confined atomic catalysts. Such supported single-atom catalysts (SAC), double-atom catalysts (DAC), and triple-atom catalysts (TAC) have made great progress in oxygen reduction reaction (ORR), nitrogen reduction reaction (NRR), and carbon dioxide reduction reaction (CO₂RR), etc.^{13–22}

In 2021, Zhang et al. theoretically discovered that incorporating transition metal (TM) atoms into the triangular hollow sites of GY at a TM loading of 43.3 wt % will lead to a spontaneous lattice reconstruction process into two-dimensional metal–carbon (2D-M₂C₁₂) honeycomb crystals.²³ They

investigated a series of 2D-M₂C₁₂ materials and found that 2D-Fe₂C₁₂ exhibited a better catalytic performance in CO oxidation (COR).^{23,24} Our previous investigations demonstrated that 2D-Fe₂C₁₂ also exhibits remarkable catalytic activity for nitrogen reduction reactions (NRR).²⁵ Up to now, there has been limited research on the application of 2D-M₂C₁₂ family materials in electrocatalysis. Besides the mentioned COR and NRR, they also have the potential to catalyze other electrocatalytic reactions, for instance, the CO₂ reduction reaction (CO₂RR). It is known that the electrochemical CO₂ reduction reaction (CO₂RR) provides a route to convert CO₂ into value-added fuels such as methane, formic acid and methanol using electricity at mild conditions.^{26–32} However, most of the current CO₂RR electrocatalysts exhibit a low catalytic activity and product selectivity. As reported in our previous study, the cooperative interaction of two adjacent individual Fe active sites could facilitate dinitrogen adsorption

Received: January 17, 2024

Revised: March 13, 2024

Accepted: April 23, 2024

Published: April 29, 2024



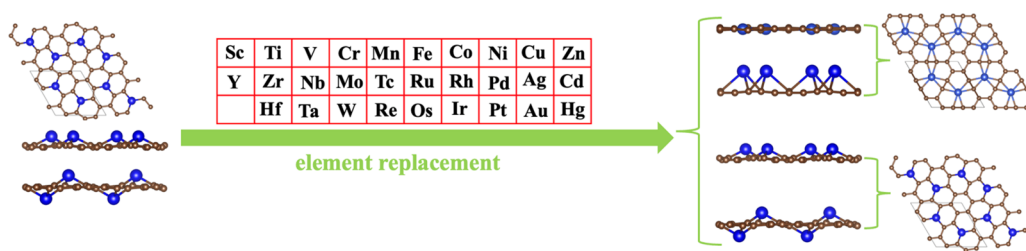


Figure 1. Schematic diagram of the construction of 2D- M_2C_{12} and the resulting configurations. Brown and blue atoms are C atoms and metal atoms, respectively.

and the following reaction process.²⁵ It is presumed that such a synergistic effect may also improve the CO_2 capture ability, and it is worth exploring the corresponding CO_2RR mechanism. Noted that 2D- M_2C_{12} is the product of lattice reconstruction when high loading of TM atoms being trapped by GY. If the TM concentration decreases, then would the self-organizing lattice reconstruction process still occur? Furthermore, what is the effect of TM concentration on the electronic structures of TM@GY and the corresponding catalytic activity?

In this study, we performed density functional theory (DFT) calculations to study the structural characteristics of a series of 2D- M_2C_{12} materials upon doping transition metal atoms (Sc to Zn, Y to Cd, and Hf to Hg) into γ -graphyne. Using an effective strategy, we screened out two potential electrocatalysts, 2D- Fe_2C_{12} and 2D- Mn_2C_{12} . Further study reveals that 1s- Mn_2C_{12} possesses high electrocatalytic activity for the CO_2 -to- CH_4 conversion. Additionally, its lower adsorption free energy for hydrogen (H) in the potential range of -0.2 to -0.8 V effectively inhibits the hydrogen evolution reaction (HER). In addition, the TM concentration can remarkably affect the electronic structures of TM@GY and the corresponding catalytic activity. When the loadings of Mn atoms exceed 27.6 wt % (4Mn), 4 adjacently distributed Mn atoms occurs, leading to the rise of the d band center, particularly for the d_z^2 center, which consequently facilitates the enhanced adsorption of CO_2 .

2. COMPUTATIONAL METHOD

All spin-polarized computations were conducted utilizing the Vienna *ab initio* simulation package (VASP), employing density functional theory (DFT) principles and the projector augmented wave (PAW) method.^{33–35} The electron–ion and exchange–correlation interactions are delineated employing the generalized gradient approximation (GGA) method, with the Perdew–Burke–Ernzerhof (PBE) functional.³⁶ van der Waals (vdW) interaction is described using empirical correction in the Grimme scheme (DFT+D3).³⁷ The kinetic energy cutoff for the plane wave is set at 500 eV, while the convergence criteria for total energy and maximum force are set at 10^{-5} eV and 0.01 eV/Å, respectively. To avoid the interaction between adjacent periodic layers in the z-direction, a vacuum layer of 20 Å is introduced. A Monkhorst–Pack mesh³⁸ with $5 \times 5 \times 1$ k-points was used for the structural optimization, and $7 \times 7 \times 1$ k-points is used for the electronic structure calculations. A 2×2 supercell containing 48 C atoms and 8 transition metal atoms is used in the calculation. The dynamic stability of the structure is verified by phonon spectra calculated by phonopy code.³⁹ *Ab initio* molecular dynamics (AIMD) simulations uses NVT ensemble and Nosé–Hoover thermostat with a time step of 2 ps and a total simulation time of 14 ps, which is used to verify the thermodynamic stability of 2D- M_2C_{12} . The climbing-image nudged elastic band (CI-NEB) method is adopted to search the transition states in CO_2RR .⁴⁰

The formation energy (E_f) of 2D- M_2C_{12} is calculated according to the following equations:

$$E_f = (E_{2D-M_2C_{12}} - 8\mu_M - 48\mu_C)/56$$

where $E_{2D-M_2C_{12}}$ is the total energy of 2D- M_2C_{12} ($M = Sc-Zn, Y-Cd, Hf-Hg$) with a 2×2 supercell, and μ_M and μ_C denote the chemical potentials of M and C atoms, respectively, which can be obtained from the bulk phase of M and GY.

The standard for the relative energy difference (ΔE_{diff}) between the 1s- M_2C_{12} and 2s- M_2C_{12} structures. The formula is as follows:

$$\Delta E_{diff} = (E(2s-M_2C_{12}) - E(1s-M_2C_{12}))/N$$

where $E(1s-M_2C_{12})$ and $E(2s-M_2C_{12})$ are the total energies and N is the total number of atoms.

The adsorption energy (E_{ad}) is expressed by

$$E_{ad} = E_{support+adsorbate} - E_{adsorbate} - E_{support}$$

where $E_{support+adsorbate}$, $E_{support}$ and $E_{adsorbate}$ represent the energy of the system after and before the adsorption of adsorbate, and the energy of the adsorbate, respectively.

The theoretical formula for calculating the loading of Mn atoms on GY can be expressed as

$$Mn(\text{wt } \%) = [(N \times 55)/(48 \times 12 + N \times 55)] \times 100\%$$

where N is the number of Mn atoms loaded in GY, 48 is the number of C atoms in the 2×2 supercell GY, and 55 and 12 are the atomic masses of Mn and C, respectively.

The constant potential method (CPM) is used to calculate the effect of the applied electrode potential on the total free energy of each elementary steps during the CO_2RR using the JDFTx code.^{41,42} The VASP-optimized structure was directly adopted in the CPM calculations with the kinetics cutoff set to 20 Hartree and the convergence criterion for the electron energy set to 3.67×10^{-6} Hartree (10^{-4} eV). The PBE functional is used in the calculations, and the DFT-D3 scheme is used to correct the long-range van der Waals interactions. The charge asymmetric nonlocal determination of local electricity (CANDEL) implicit solvation model⁴³ is used to depict the aqueous solution. The free energy change for each reaction step is calculated by⁴²

$$\Delta G_{CPM} = G(I2) - G(I1) - G(H_2(g))/2 + |e|U - (q1 - q2)\mu e$$

where $G(I2)$ and $G(I1)$ represent the free energy of the intermediate product at the corresponding potential after and before the reaction, respectively, $G(H_2(g))$ donated the free energies of hydrogen. U is the applied voltage versus standard hydrogen electrode (SHE), and μe is the electron energy defined by the absolute electrode potential, where $U = \mu e - \mu_{SHE}$.

3. RESULTS AND DISCUSSION

3.1. Screening of Potential Electrocatalyst in 2D- M_2C_{12} . Based on the reported 1s- Fe_2C_{12} and 2s- Fe_2C_{12} configurations,²⁵ we investigated the structural energetics of a series of 2D- M_2C_{12} ($M = Sc-Zn, Y-Cd, Hf-Hg$) by M element substitution method, as illustrated in Figure 1. For simplicity, the configuration in which the transition metal atoms are located on one side of the carbon skeleton is called 1s- M_2C_{12} , and the one on two sides is named as 2s- M_2C_{12} . The

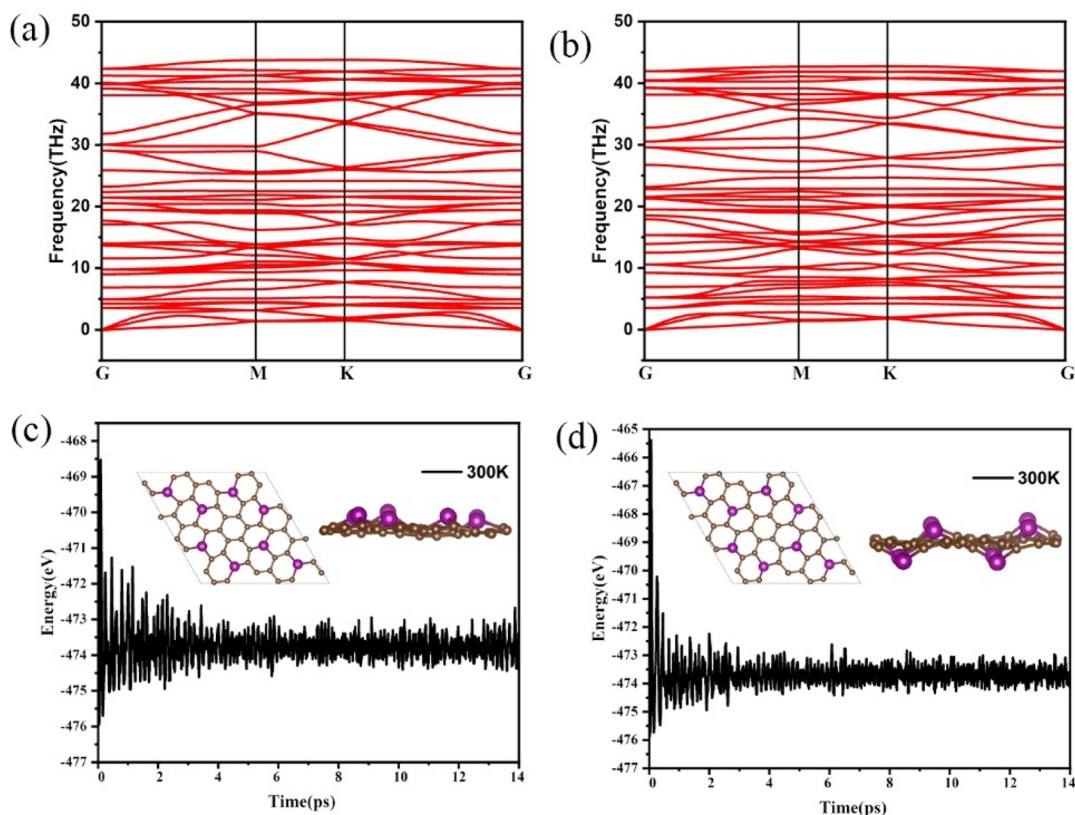


Figure 2. Phonon spectra of (a) $1s\text{-Mn}_2\text{C}_{12}$ and (b) $2s\text{-Mn}_2\text{C}_{12}$. Diagrams of the total energy changing with time at 300 K obtained by AIMD calculation for (c) $1s\text{-Mn}_2\text{C}_{12}$ and (d) $2s\text{-Mn}_2\text{C}_{12}$.

optimized structures for the substituted $2\text{D-Cd}_2\text{C}_{12}$, $2\text{D-Hg}_2\text{C}_{12}$, $1s\text{-Cu}_2\text{C}_{12}$, $1s\text{-Ag}_2\text{C}_{12}$, and $1s\text{-Au}_2\text{C}_{12}$ revert back to the framework of GY, indicating the relatively weak interaction between the M and C atom. For $1s\text{-Cu}_2\text{C}_{12}$, it is a planar structure, with Cu atoms positioned at the center of the carbon framework. As for $2\text{D-Cd}_2\text{C}_{12}$ and $2\text{D-Hg}_2\text{C}_{12}$, the perpendicular distances between Cd and Hg and the carbon framework are $\sim 3.08/3.14$ Å (one side/two sides) and $\sim 3.20/3.16$ Å (one side/two sides), respectively. This indicates that these two metal elements cannot be stably adsorbed onto the carbon framework and will not be studied further. For $1s\text{-Ag}_2\text{C}_{12}$ and $1s\text{-Au}_2\text{C}_{12}$, the perpendicular distances between Ag and Au atoms and the carbon skeleton are ~ 1.66 and ~ 0.72 Å, respectively. For convenience, we still adopt the name criteria of $1s\text{-M}_2\text{C}_{12}$ or $2s\text{-M}_2\text{C}_{12}$ for the above-mentioned five configurations, although they do not belong to the $2\text{D-M}_2\text{C}_{12}$ family. These seven optimized configurations are consistent with the structural optimization of transition metal atoms doped on all triangular hollow sites of GY.

In general, a good electrocatalyst should facilitate the transfer of electrons between the catalyst and the reactant, and the synthesis in an experiment should be feasible. Therefore, we developed an effective strategy for potential electrocatalyst screening in $2\text{D-M}_2\text{C}_{12}$ materials. First, we calculate the formation energy and energy differences of structural isomers to determine the relative stability of $2\text{D-M}_2\text{C}_{12}$. As shown in Figure S1, based on the formation energy of $1s\text{-Fe}_2\text{C}_{12}$ and the relative energy difference $|\Delta E_{\text{diff}}| = 10$ meV/atom as the criteria, 13 candidates were identified from the initial 58 structures. Then, we perform electronic structure calculations to screen the metallic or half-metallic $2\text{D-M}_2\text{C}_{12}$. As shown in

Figure S2, apart from $2\text{D-Fe}_2\text{C}_{12}$, seven structures exhibiting metallic or half-metallic properties were obtained in this step. Additionally, $1s\text{-Mn}_2\text{C}_{12}$ and $2s\text{-Mn}_2\text{C}_{12}$ exhibit magnetic behavior with magnetic moments of 2.40 and 2.01 μ_B per unit cell, respectively. As shown in Figure S3, the spin densities are mainly localized on the Mn atoms. Generally, atoms with high localized states are active sites for catalytic reaction. The others are categorized as semiconductors, as outlined in Table S1. We also calculated the electronic band structure of these configurations using the DFT+ U method ($U_{\text{eff}} = 3$ eV).⁴⁴ As shown in Figure S4, except for $2s\text{-Mn}_2\text{C}_{12}$ which transitions from a semimetal to a metallic character, the electronic properties of the other structures remain unchanged. Our goal is to identify potential catalysts with metallic or half-metallic properties. Therefore, the variations in $2s\text{-Mn}_2\text{C}_{12}$ do not affect our results. Finally, we estimate the kinetic and thermodynamic stabilities of these potential candidates. As shown in Figures 2a,b and S5, only $1s\text{-Mn}_2\text{C}_{12}$ and $2s\text{-Mn}_2\text{C}_{12}$ are dynamically stable without imaginary phonon modes. Furthermore, 14 ps *ab initio* molecular dynamics (AIMD) simulations at 300 and 500 K (see Figures 2c,d and S6) revealed that both $1s\text{-Mn}_2\text{C}_{12}$ and $2s\text{-Mn}_2\text{C}_{12}$ maintain structural integrity over time, thereby confirming their good thermodynamic stability. In summary, the aforementioned analyses demonstrated that both $1s\text{-Mn}_2\text{C}_{12}$ and $2s\text{-Mn}_2\text{C}_{12}$ are kinetically and thermodynamically stable, making them promising candidates as electrocatalysts for further study.

3.2. Adsorption and Activation of CO_2 on $2\text{D-Mn}_2\text{C}_{12}$.

In a catalytic reaction, the effective adsorption of adsorbates is the prerequisite. Therefore, we studied the adsorption of CO_2 on the newly screened $2\text{D-Mn}_2\text{C}_{12}$ and the reported 2D-

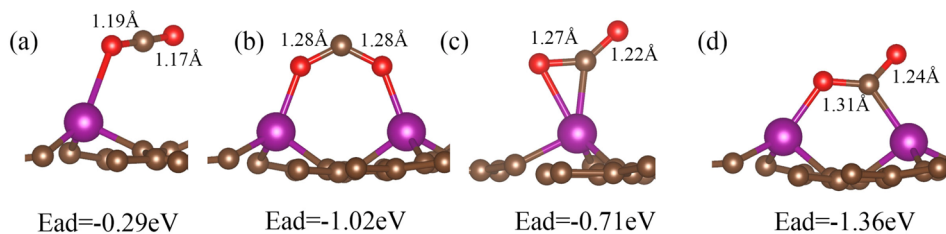


Figure 3. (a–d) CO₂ adsorption on 1s-Mn₂C₁₂ with different adsorption modes: end-on, bridge-on, side-on, and bidentate.

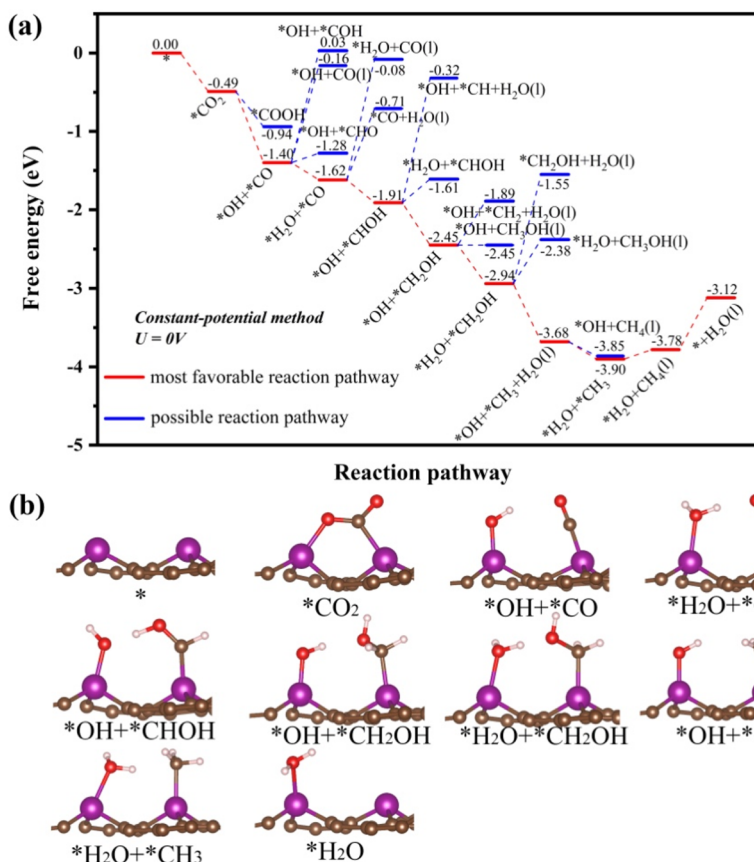


Figure 4. (a) Calculated free energy diagram of the reduction of CO₂ on 1s-Mn₂C₁₂ at an applied potential of 0 V and (b) its intermediate structures.

Fe₂C₁₂. For 1s-Mn₂C₁₂, as depicted in Figure 3, four typical adsorption configurations of CO₂ were considered, including one physical adsorption and three chemical adsorptions. In the physical adsorption, only one Mn atom is involved in the adsorption process, and it takes an end-on adsorption mode; the corresponding adsorption energy is only -0.29 eV, indicating a weak Mn–O interaction. In the side-on adsorption mode, the adsorption energy of CO₂ is -0.71 eV, which suggests that CO₂ can be efficiently captured. When two Mn atoms work together to capture CO₂, the collective effect significantly enhances CO₂ adsorption, and the maximum adsorption energy could reach -1.36 eV for the bidentate mode, forming Mn–O and Mn–C bond. The effectiveness of CO₂ activation can be directly inferred from the changes in the C–O bond and the \angle OCO angle within the CO₂ molecule, as depicted in Figure 3. It can be seen that the C–O bond length within CO₂ extends from 1.16 Å to 1.19/1.17 Å, 1.28/1.28 Å, 1.27/1.22 Å, and 1.31/1.24 Å, respectively. Simultaneously, the \angle OCO angle decreases from 180° to 177.81°, 126.23°, 141.29°, and 128.53°.

Moreover, Bader charge calculations reveal that the charge transfers from the substrate to the adsorbed CO₂ molecules are 0.05, 0.89, 0.66, and 0.90 e, respectively. These observations are consistent with the calculated differential charge density diagram (depicted in Figure S7). Specifically, Mn atoms are in proximity to adsorbed CO₂ molecules and subsequently form Mn–O bonds or Mn–C bonds with the adsorbed CO₂.

Additionally, we evaluated the transition barriers for the physisorbed CO₂ to its chemisorbed configurations using the climbing-image nudged elastic band (CI-NEB) method, as depicted in Figure S8. Encouragingly, the transition energy barriers from the physisorbed end-on configuration to the bridge-on, side-on, and bidentate configurations are 0.03, 0.09, and 0.02 eV, respectively. Such low energies suggest that these transition processes can be effortlessly overcome under room temperature conditions. For 2s-Mn₂C₁₂, the distance between adjacent Mn atoms on the same side is as large as 6.76 Å, the absence of cooperative interaction results in relative weaker

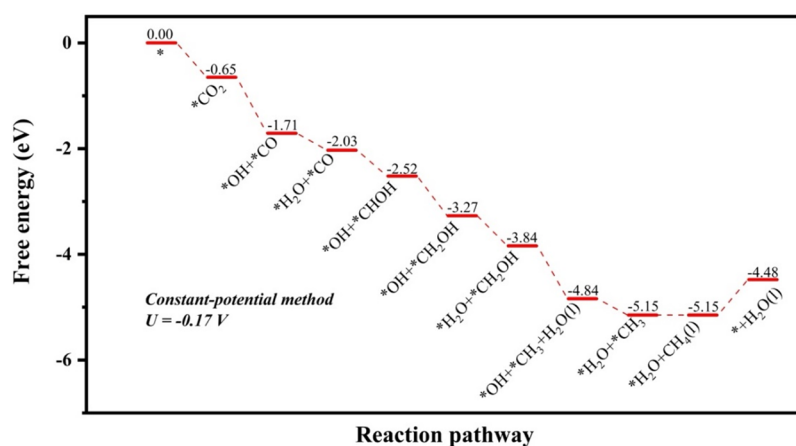


Figure 5. Calculated free energy diagram of the reduction of CO_2 on $1s\text{-Mn}_2\text{C}_{12}$ at an applied potential of -0.17 V.

adsorption of CO_2 . As depicted in Figure S9, the adsorption energies of CO_2 in the end-on and side-on configurations are -0.40 and -0.83 eV respectively.

Similar adsorption behavior was observed for $2\text{D-Fe}_2\text{C}_{12}$, as detailed in Figure S9. The adsorption energies of CO_2 on $1s\text{-Fe}_2\text{C}_{12}$ takes the end-on, side-on, bridge-on, and bidentate configurations are -0.30 , -0.55 , -0.77 , and -1.09 eV, respectively. For $2s\text{-Fe}_2\text{C}_{12}$, the adsorption energies of CO_2 in the end-on and side-on configurations are -0.34 and -0.53 eV, respectively. Since $2\text{D-Mn}_2\text{C}_{12}$ shows stronger CO_2 binding ability, we select it as the most promising candidate for catalyzing the following electrochemical reduction of CO_2 .

3.3. Electrochemical Reduction of CO_2 on $2\text{D-Mn}_2\text{C}_{12}$.

Based on the most stable CO_2 adsorption configuration, the electrochemical CO_2 reduction reaction pathway is investigated by using the constant potential method (CPM) in the JDFTx software, as shown in Figure 4. The intermediates of the CO_2RR are obtained through VASP optimization, and the effects of solvation and the applied potential are evaluated using JDFTx software. From this, one can see that the adsorption free energy of CO_2 on $1s\text{-Mn}_2\text{C}_{12}$ is -0.49 eV. In the first hydrogenation step, the adsorbed CO_2 can be reduced to $^*\text{COOH}$ or $^*\text{OCHO}$. The formation of $^*\text{COOH}$ by H atoms attacking the O that is not connected to Mn at the far end of $^*\text{CO}_2$ is an energetically favorable downhill process, and the free energy is reduced by 0.45 eV. And when the H proton attacks the other O, that is, the adsorbed O in $^*\text{CO}_2$, it causes the cleavage of the C–O bond and produces $^*\text{OH} + ^*\text{CO}$, resulting in a substantial drop in free energy of 0.91 eV. Through AIMD simulations with explicit solvation model consists of 23 water molecules and one H_3O molecule, we observed a similar phenomenon, as shown in Figure S10, the combination of H in H_3O and $^*\text{CO}_2$ leads to bond-breaking of the C–O bond, resulting in the formation of $^*\text{OH} + ^*\text{CO}$. For the formation of $^*\text{OCHO}$, this hydrogenation process encounters geometric frustration, which involves the Mn–C bond breaking and the generation of the Mn–O bond. Such a phenomenon has also been observed in the CO_2RR catalyzed by some dual-atom catalysts.^{45,46} As shown in Figure S11, such a process requires one to overcome an energy barrier of 1.21 eV, indicating the formation of $^*\text{OCHO}$ is difficult. Therefore, the first hydrogenation step prone the formation of $^*\text{OH} + ^*\text{CO}$. In the second hydrogenation step, H protons exhibit a preference for reacting with $^*\text{OH}$ to form $^*\text{H}_2\text{O} + ^*\text{CO}$, resulting in a decrease in free energy by 0.22 eV. Compared to

other alternative pathways, they are all accompanied by an increase in free energy. The desorption of H_2O and CO from generated $^*\text{H}_2\text{O} + ^*\text{CO}$ requires free energies of 0.91 and 1.54 eV, respectively, indicating the direct desorption process is energy unfavorable. Then, we considered the further hydrogenation of $^*\text{CO}$ to produce $^*\text{H}_2\text{O} + ^*\text{CHO}$ or $^*\text{H}_2\text{O} + ^*\text{COH}$. However, the optimized hydrogenation products are both $^*\text{OH} + ^*\text{CHOH}$ due to the H transfer in $^*\text{H}_2\text{O}$. In the AIMD simulations with the explicit solvation model at 300 K (shown in Figure S12), it is observed that $^*\text{CO}$ first acquires a H atom from H_3O , forming $^*\text{H}_2\text{O} + ^*\text{CHO}$. Then, the H atom from the adsorbed $^*\text{H}_2\text{O}$ transfers to $^*\text{CHO}$, forming $^*\text{OH} + ^*\text{CHOH}$. Therefore, $^*\text{OH} + ^*\text{CHOH}$ is a reasonable intermediate during the reduction process. From the energy point of view, the most likely fourth hydrogenation step is the hydrogen proton pair interacting with the C atom in $^*\text{CHOH}$ to form $^*\text{OH} + ^*\text{CH}_2\text{OH}$ ($\Delta G = -0.54$ eV) rather than yielding $^*\text{OH} + ^*\text{CH} + \text{H}_2\text{O}(\text{l})$ ($\Delta G = 1.59$ eV) or $^*\text{H}_2\text{O} + ^*\text{CHOH}$ ($\Delta G = 0.30$ eV). The following reduction of $^*\text{OH} + ^*\text{CH}_2\text{OH}$, which may lead to $^*\text{H}_2\text{O} + ^*\text{CH}_2\text{OH}$ ($\Delta G = -0.49$ eV), $^*\text{OH} + \text{CH}_3\text{OH}(\text{l})$ ($\Delta G = 0.00$ eV) or $^*\text{OH} + ^*\text{CH}_2 + \text{H}_2\text{O}(\text{l})$ ($\Delta G = 0.56$ eV). Clearly, the hydrogen proton pair prefers to interact with $^*\text{OH}$. Due to the existence of hydrogen bonding, the direct desorption of H_2O in $^*\text{H}_2\text{O} + ^*\text{CH}_2\text{OH}$ requires an energy input of 1.39 eV. Then we evaluate the following reduction of $^*\text{H}_2\text{O} + ^*\text{CH}_2\text{OH}$, and it involves the participation of a hydrogen proton pair and the H atom in adsorbed H_2O . Initially, the hydrogen protons attack the O atom in $^*\text{CH}_2\text{OH}$ to produce $^*\text{H}_2\text{O} + ^*\text{CH}_2 + \text{H}_2\text{O}(\text{l})$, followed by the H atom transfer from $^*\text{H}_2\text{O}$ to $^*\text{CH}_2$, leading to the formation of $^*\text{OH} + ^*\text{CH}_3 + \text{H}_2\text{O}(\text{l})$ ($\Delta G = -0.74$ eV). After performing 300 K AIMD simulations with the explicit solvation model (shown in Figure S13), it was observed that the hydrogen atom in the H_2O cluster transfers to $^*\text{CH}_2\text{OH}$, resulting in the formation of $^*\text{CH}_2$ and the dissociation of H_2O . In addition, the free energy of hydrogenation to form $^*\text{H}_2\text{O} + \text{CH}_3\text{OH}(\text{l})$ from $^*\text{H}_2\text{O} + ^*\text{CH}_2\text{OH}$ rises by 0.56 eV, indicating that the hydrogenation of $^*\text{H}_2\text{O} + ^*\text{CH}_2\text{OH}$ does not produce $^*\text{H}_2\text{O} + \text{CH}_3\text{OH}(\text{l})$. In the seventh hydrogenation step, hydrogen proton pairs again preferentially interact with $^*\text{OH}$ to generate $^*\text{H}_2\text{O} + ^*\text{CH}_3$ ($\Delta G = -0.22$ eV) rather than hydrogenation of $^*\text{CH}_3$ to form $^*\text{OH} + \text{CH}_4(\text{l})$ ($\Delta G = -0.17$ eV). The final hydrogenation step is the generation of $\text{CH}_4(\text{l})$, which is endothermic by 0.12 eV. Finally, $^*\text{H}_2\text{O}$ desorption is an endothermic process with a free

energy increase of 0.66 eV. For the entire reaction process, the potential-determining step (PDS) is the hydrogenation of $*\text{H}_2\text{O} + *\text{CH}_3$ to $*\text{H}_2\text{O} + \text{CH}_4(\text{l})$ ($\Delta G = 0.12$ eV).

Additionally, we assessed the potential effect on the aforementioned potential-determining step ($*\text{H}_2\text{O} + *\text{CH}_3$ to $*\text{H}_2\text{O} + \text{CH}_4(\text{l})$). When the applied potential is set to -0.12 V, the ΔG for PDS is 0.04 eV. Therefore, what is the least potential for overcoming the rise of free energy for the PDS? Based on prior research, a linear relationship is observed between the applied potential and the free energy difference for an elementary step.^{47,48} Therefore, we randomly choose a potential of -0.48 V to see the free energy difference for the PDS, and it turns out to be -0.22 eV. Using the results obtained at 0, -0.12 , and -0.48 V, we fit the relationship between the applied potential and the free energy difference, as plotted in Figure S14. According to the fitted linear relationship, the least potential should be -0.17 V. Then, we further calculated the free energy diagram for the optimal pathway at -0.17 V, as illustrated in Figure 5. In this diagram, all reduction processes are downhill in energy. Based on our calculations, the screened $1s\text{-Mn}_2\text{C}_{12}$ could serve as an outstanding electrocatalyst for CO_2 -to- CH_4 conversion, and its catalytic performance is better than most of the reported CO_2RR electrocatalysts, such as Cr-GY (-0.29 V),²¹ Fe-GDY (-0.43 V),¹⁷ and NiNi-GDY (-0.28 V),⁴⁹ and comparable to the catalytic performance of Mo_2TiC_2 (-0.17 V).⁵⁰

In addition, the CO_2 reduction path of $2s\text{-Mn}_2\text{C}_{12}$ was also evaluated, as shown in Figure S15. The adsorption free energy of CO_2 in the side-on configuration is -0.15 eV, and the first step of hydrogenation to form $*\text{OCHO}$ releases -1.13 eV of energy. In the second step, $*\text{OCH}_2\text{O}$ is formed by hydrogenation, and the free energy of the hydrogenation step increases by 0.62 eV. The subsequent hydrogenation to form $*\text{OCH}_2\text{OH}$ releases 1.00 eV. The fourth hydrogenation step generates $*\text{OCH}_2 + \text{H}_2\text{O}(\text{l})$, with the free energy rising by 0.36 eV. Then the generated $*\text{OCH}_2$ will be further hydrogenated to $*\text{OCH}_3$, and the free energy of this hydrogenation process decreases by 1.07 eV. The free energy of the next hydrogenation to form $* + \text{CH}_3\text{OH}(\text{l})$ will rise by 0.82 eV, while the formation of $*\text{O} + \text{CH}_4(\text{l})$ will release 0.41 eV; the latter one would be more energy favored. The free energies of the subsequent two hydrogenations to form $*\text{OH}$ and $*\text{H}_2\text{O}$ decrease by 0.75 and 0.21 eV, respectively. The desorption of the finally generated H_2O requires an energy of 0.79 eV. For the entire CO_2RR reaction process on $2s\text{-Mn}_2\text{C}_{12}$, the hydrogenation of $*\text{OCHO}$ to form $*\text{OCH}_2\text{O}$ ($\Delta G = 0.62$ eV) is PDS, which is much higher than that of PDS on $1s\text{-Mn}_2\text{C}_{12}$, indicating the relatively low catalytic activity toward CO_2 -to- CH_4 conversion.

3.4. Kinetic Process during CO_2RR . It is widely recognized that kinetic barriers play a pivotal role in elementary reactions. For the electrochemical carbon dioxide reduction reaction (CO_2RR), the hydrogenation process involves the sequential addition of protons and electrons. In computational studies, the proton–electron pair ($\text{H}^+ + \text{e}^-$) is often employed as an approximation for electrochemical hydrogenation. In this study, we evaluated only the kinetic energy barriers of the CO_2RR process for the superior catalytic performance of $1s\text{-Mn}_2\text{C}_{12}$. The pathways for the eight proton-coupled electron transfers are listed in Table S2. To evaluate the corresponding kinetic energy barriers, various hydrogen sources are introduced herein. Initially, we utilized a dissociated neutral H atom to mimic a proton. The kinetic

energy barriers of the hydrogenation process in the CO_2RR are shown in Figure S16. Throughout the process, the first ($*\text{CO}_2 + (\text{H}^+ + \text{e}^-) \rightarrow *\text{OH} + *\text{CO}$), second ($*\text{CO} + *\text{OH} + (\text{H}^+ + \text{e}^-) \rightarrow *\text{H}_2\text{O} + *\text{CO}$), and fifth ($*\text{CH}_2\text{OH} + *\text{OH} + (\text{H}^+ + \text{e}^-) \rightarrow *\text{H}_2\text{O} + *\text{CH}_2\text{OH}$) hydrogenation steps have relatively higher energy barriers compared to the other steps, measuring 1.21, 1.17, and 1.15 eV, respectively. Among them, the process of hydrogenation of $*\text{H}_2\text{O} + *\text{CH}_2\text{OH}$ into $*\text{OH} + *\text{CH}_3 + \text{H}_2\text{O}$ is divided into two steps: $*\text{H}_2\text{O} + *\text{CH}_2\text{OH} \rightarrow *\text{OH} + *\text{CH}_2 + \text{H}_2\text{O}(\text{l})$, $*\text{OH} + *\text{CH}_2 + (\text{H}^+ + \text{e}^-) \rightarrow *\text{OH} + *\text{CH}_3$. For these three processes with relatively larger energy barriers, the H_3O^+ model is further introduced to estimate the corresponding energy barrier. We adjusted the charge of the entire system by subtracting one electron to create a positively charged system. As shown in Figures S17–19, the energy barriers for these three hydrogenation processes are relatively lower, with the highest energy barrier of 0.37 eV for the second hydrogenation step. Based on these comprehensive calculations, it is plausible to infer that the kinetic process of electrochemical hydrogenation remains feasible throughout the entire electrochemical CO_2RR .

3.5. Selectivity of $1s\text{-Mn}_2\text{C}_{12}$. It is known that the hydrogen evolution reaction (HER) is a primary competing reaction during the CO_2 reduction reaction, and the competitive adsorption of CO_2 and H_2O should also be considered. As shown in Figure 6, the adsorption free energies

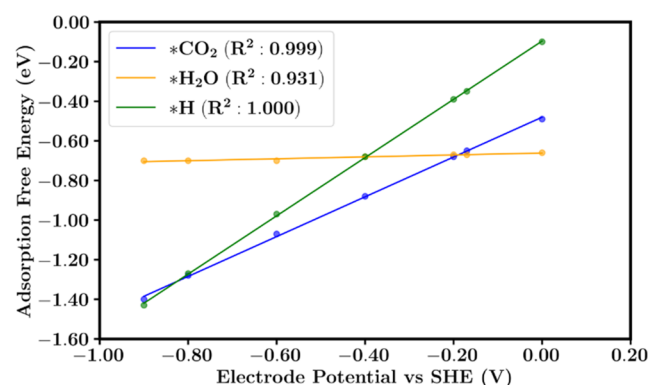


Figure 6. Calculated adsorption free energies of H atoms, CO_2 molecules, and H_2O under different applied potentials.

of the adsorbates are linearly related to the electric potential. As the potential becomes more negative, the adsorption free energy of the adsorbates also becomes more negative. Among these, the H_2O molecules exhibit less sensitivity to potential changes compared to the others. When the potential is greater than -0.2 V, the adsorption of H_2O becomes more favorable, while at potentials below -0.8 V, H proton adsorption dominates. The optimal adsorption of CO_2 occurs between -0.2 V and -0.8 V, ensuring its preferential absorption, which is advantageous for the CO_2RR process.

3.6. Effects of Different Mn Atom Loadings on Electronic Properties and Catalytic Activity. In section 3.2, we discovered that the synergistic interaction between two adjacent Mn atoms on the $1s\text{-Mn}_2\text{C}_{12}$ monolayer enhances the adsorption of CO_2 . Therefore, a question arises here: can the adsorption of CO_2 be promoted by loading only two adjacent Mn atoms on GY? To address it, we constructed a 2×2 supercell GY with two adjacent Mn atoms located in the triangular hollow sites for testing, and it was found that the

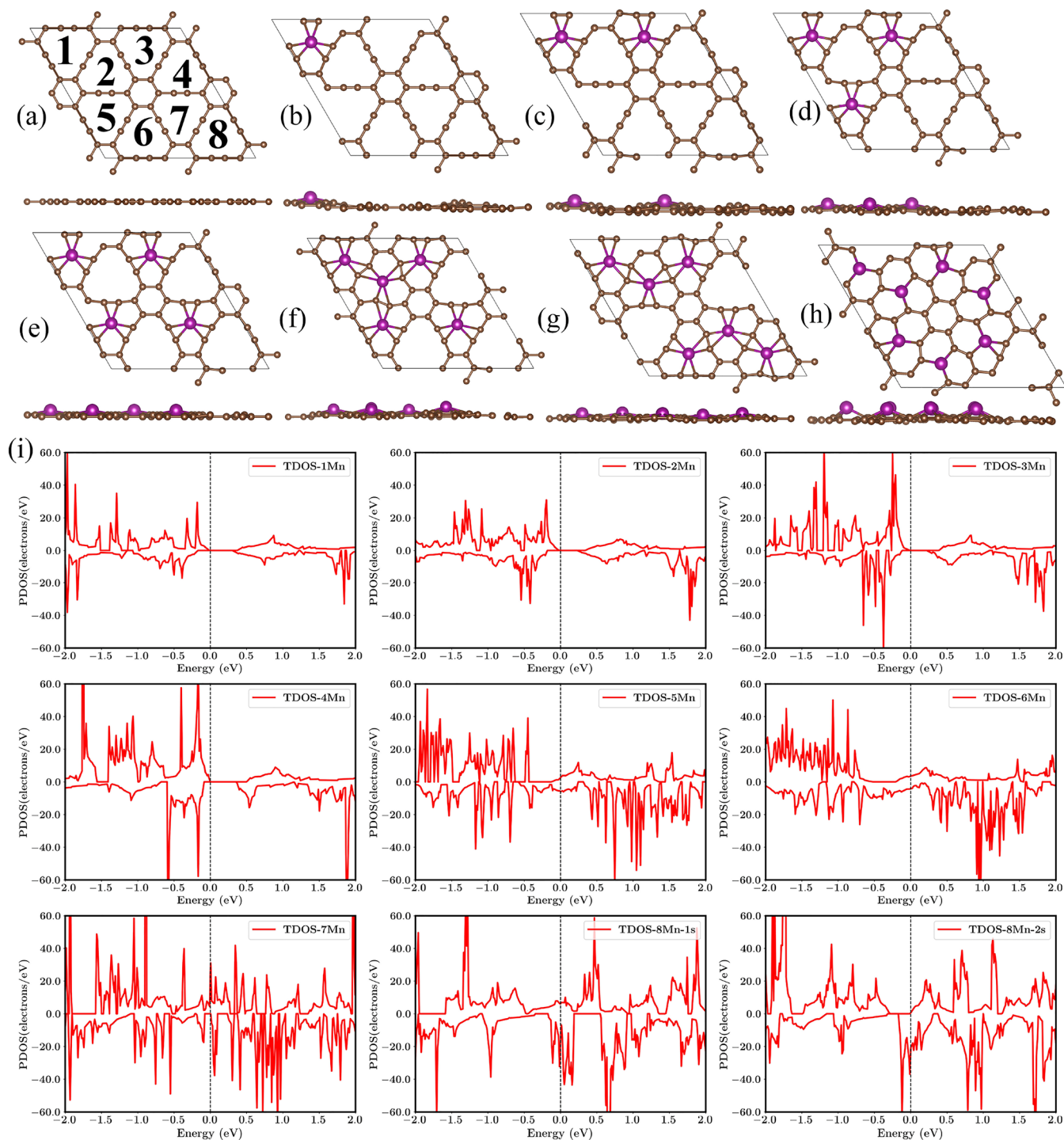


Figure 7. Lowest energy configuration with different Mn loadings. The numbers in (a) represent the serial number. (b)–(h) are 1Mn-1, 2Mn-13, 3Mn-135, 4Mn-1357, 5Mn-12357, 6Mn-123678, and 7Mn-1234567 respectively. (i) Density of states diagram of structures with different Mn loadings.

adsorption energy of CO_2 is 0.02 eV. This indicates that the presence of two adjacent Mn atoms is not ascribed for the strong adsorption capacity for CO_2 , and what is the intrinsic activation mechanism? Note that 1s-Mn₂C₁₂ is an isomerized structure formed by loading 8 Mn atoms on 2×2 supercell GY with the highest loading of Mn atoms (43.3 wt %), and it exhibits a strong adsorption capacity for CO_2 (−1.36 eV). While for the low loading of Mn atoms (16 wt %, 2Mn), its adsorption energy of CO_2 is only 0.02 eV. Could this possibly

be attributed to the variation in the concentration of Mn atoms?

By changing the loading of Mn atoms on 2×2 supercell GY from 8.7 wt % (1Mn) to 40.1 wt % (7Mn), we studied their adsorption energies of CO_2 at different TM concentrations. According to the symmetry of 2×2 supercell GY, a total of 20 different structures are obtained, and we named them NMn-X, where N represents the number of Mn atoms and X represents the index of the loaded pore. There are eight triangular pores

in 2×2 supercell GY for TM loading, as shown in Figure 7(a). For example, 4Mn-1357 represents the loading of 4 Mn atoms into pore nos. 1, 3, 5, and 7. For convenience, 1s-Mn₂C₁₂ and 2s-Mn₂C₁₂ are labeled as 8Mn-1s and 8Mn-2s. In Figure 7(b–h), we give the lowest energy configurations at different Mn loadings. The formation energies of the most stable structures under different loadings are plotted in Figure S20. It is found that the formation energy increases linearly as the increase of Mn loadings, and it reaches the highest value of 0.09 eV per atom at 40.1 wt % (7Mn), and it decreases to \sim 0.08 eV per atom when the loading of Mn reaches 43.3 wt % (8Mn). Due to the repulsive forces between d-orbitals, the doping Mn atoms prefer locating at the nonadjacent triangular pores, and thereby the most stable configurations for 1Mn, 2Mn, 3Mn, and 4Mn take the dispersed arrangement. When the Mn loading exceeds 27.6 wt % (4Mn), adjacent Mn atoms appear, leading to partial distortion of the C \equiv C bonds. With the Mn loading further increases to 43.3 wt % (8Mn), GY undergoes isomerization into 8Mn-1s and 8Mn-2s. The obtained electronic properties of these structures are shown in Figure 7(i). From it, one can see that 1Mn-1, 2Mn-13, 3Mn-135, and 4Mn-1357 are semiconducting, 5Mn-12357 and 6Mn-123678 are metallic, while 7Mn-1234567 is half-metallic. When the loading amount of Mn increases from 8.7 wt % (1Mn) to 27.6 wt % (4Mn), the average number of electrons lost by each Mn atom is 0.87 e. As the loading amount increases from 32.3 wt % (5Mn) to 43.3 wt % (8Mn), the average number of electrons lost by each Mn atom increases to 0.91, 0.92, 0.89, and 0.88 e, respectively. Compared with the nonadjacent systems, the interaction between adjacent Mn atoms causes the increased charge transfer between Mn atoms and the GY substrate, changing the electron distribution of GY, making the Mn@GY become metallic or half-metallic, which is confirmed from the calculated projected density of states (PDOS) diagram (Figure S21) that the PDOS of the GY substrate crosses the Fermi level as Mn loadings higher than 27.6 wt % (4Mn).

Furthermore, we calculated the CO₂ adsorption on Mn@GY at different Mn loadings. As shown in Figure S22, the structures from 1Mn-1 to 4Mn-1357 can only undergo physisorption of CO₂ since only one Mn atom participating in the adsorption of CO₂, and the adsorption energy is around $-$ 0.17 eV. For Mn loading ranging from 32.3 wt % (5Mn) to 43.3 wt % (8Mn), their adsorption energies for CO₂ are $-$ 0.52 (5Mn-12357), $-$ 0.44 (6Mn-123678), $-$ 1.27 (7Mn-1234567), $-$ 1.37 (8Mn-1s), and $-$ 0.83 eV (8Mn-2s), respectively, with the strongest adsorption energy observed for 8Mn-1s. For the range of loadings from 32.3 wt % (5Mn) to 43.3 wt % (8Mn), although two Mn atoms cooperation occurs, the adsorption capacity for CO₂ is different.

To better understand the activation mechanism of CO₂ adsorption, we compared the d orbitals of Mn atoms and the 2p orbitals of CO₂ before and after 8Mn-1s adsorption. It can be seen from Figure S23 that the HOMO ($1\pi_g$) orbit of the CO₂ molecule transfers electrons to the empty d orbital of Mn, and then the electrons in the occupied orbit of Mn donates electrons back to the LUMO orbit ($2\pi_u$) of CO₂. From the differential charge density diagram (Figure S7(d)), the d_z^2 orbital of Mn and the 2p orbital of CO₂ that play a role in the adsorption of CO₂ and the p_z orbital of the twisted C \equiv C bonds (abbreviated as CC) also participates. Similar phenomenon is also found in the differential charge density (in Figure S24) plots of CO₂ adsorbed on 5Mn-12357, 6Mn-123678, and 7Mn-1234567. By investigating the d_z^2 orbitals

near the Fermi level in these four structures (Figure S25), it is observed that a rise in the d_z^2 electronic state near the Fermi level is beneficial for CO₂ adsorption. Among the four structures, 6Mn-123678 exhibits the fewest electronic states near the Fermi level, resulting in the weakest CO₂ adsorption capability. This is supported by examining the d_z^2 centers of the two Mn atoms involved in adsorption (Mn1/Mn2) as shown in Table S3. The closest d_z^2 centers to the Fermi level are 8Mn-1s (values of Mn1/Mn2 are $-$ 0.983/ $-$ 0.983), followed by 7Mn-1234567 ($-$ 1.012/ $-$ 0.985), 5Mn-12357 ($-$ 1.447/ $-$ 1.129), and finally 6Mn-123678 ($-$ 1.441/ $-$ 1.429). Similarly, we also investigated the p_z centers of the CC atoms in these four structures. The p_z center in 8Mn-1s ($-$ 0.940) is the closest to the Fermi level among them, followed by 7Mn-1234567 ($-$ 1.029), 5Mn-12357 ($-$ 1.095), and 6Mn-123678 ($-$ 1.122). Based on these results, the d_z^2 orbitals of Mn are crucial for the adsorption of CO₂, and the p_z orbitals of CC also play a minor role in this process. Noted that except for 6Mn-123678, all the others have four neighboring Mn atoms. Whether this distribution of four neighboring Mn atoms could enhance the adsorption of CO₂?

To verify our guess, we used a relatively larger 3×3 supercell GY loaded with 4Mn (Mn4@ 3×3 -GY), as shown in Figure S26. The adsorption energy of CO₂ by Mn4@GY is $-$ 0.62 eV. The adjacent arrangement of four Mn atoms causes a distortion of the C \equiv C bonds between two adjacent Mn atoms. Compared with the normal C \equiv C bonds (called CC4), the twisted C \equiv C bonds (called CC1, CC2, and CC3, as shown in Figure S26(a)) have stronger interactions with Mn atoms, changing the p_z orbitals electron distribution (Figure S26(b)). The p_z band center of CC4 ($-$ 1.084) is farther away from the Fermi level than the other three (CC1: $-$ 0.992, CC2: $-$ 0.993, CC3: $-$ 0.960). The adjacent arrangement of four Mn atoms makes the d_z^2 center of the central Mn2 atom higher than the other three Mn atoms (in Table S4), which is beneficial for the adsorption of CO₂. When 2 Mn atoms are loaded on the adjacent triangular pores of 3×3 supercell GY, the adsorption energy of CO₂ is only $-$ 0.02 eV, which is much positive than the adsorption energy of CO₂ on 4 Mn atoms with adjacent arrangement mode. This is because the d_z^2 center of the Mn atom and the p_z center of the 4 CC atoms of Mn4@GY are higher than those of Mn2@ 3×3 -GY (in Table S4). The above results show that the four adjacent Mn atoms will increase their own d_z^2 center and change the p_z center of the CC atom, thereby improving the CO₂ capture ability.

In general, Mn@GY undergoes a transition from a semiconductor into a metallic or half-metallic state at a relatively higher Mn loading (27.6 wt % for 2×2 supercell GY). The adjacent arrangement of four Mn atoms leads to the rise of the d_z^2 center of the Mn atom and the p_z center of the CC atom, thereby facilitating improved CO₂ adsorption.

4. CONCLUSIONS

In this study, we designed an effective strategy to find electrocatalysts from a series of 2D-M₂C₁₂ materials. Through first-principles calculations, we found that 1s-Mn₂C₁₂ is an excellent catalyst with high selectivity and low applied potential for the CO₂RR. In addition, we also studied the properties of Mn@GY with different Mn loadings. The Mn@GY is a semiconductor at a relative low TM loading (8.7 wt % to 27.6 wt %), while it turns into a metal or half-metal at relative higher TM loadings (32.3 wt % to 43.3 wt %). Under higher Mn loading, four adjacently arranged Mn atoms increase their

own d_z^2 center and redistribute the p_z arrangement in the $C\equiv C$ bonds. The rise of the d_z^2 center of Mn atoms and p_z center of CC atoms are beneficial for the adsorption of CO_2 . Finally, our findings offer valuable insights and serve as a guiding reference for the development of more efficient and sustainable electrocatalysts for the CO_2RR .

■ ASSOCIATED CONTENT

SI Supporting Information

The Supporting Information is available free of charge at <https://pubs.acs.org/doi/10.1021/acsami.4c00973>.

Obtained cohesive energies, formation energies, CO_2 adsorption energy, d band center, d_z^2 center, p_z center, band structures, PDOS, AIMDs, phonon spectrum, differential charge density, calculated MEP for CO_2RR , Free energy diagrams in related systems (PDF)

■ AUTHOR INFORMATION

Corresponding Author

Xinrui Cao – Department of Physics and Fujian Provincial Key Laboratory of Theoretical and Computational Chemistry, Xiamen University, Xiamen 361005, China; orcid.org/0000-0002-2998-8863; Email: xinruicao@xmu.edu.cn

Authors

Yaowei Xiang – Department of Physics, Xiamen University, Xiamen 361005, China
Wengeng Chen – Department of Physics, Xiamen University, Xiamen 361005, China
Meijie Wang – Department of Physics, Xiamen University, Xiamen 361005, China
Zi-Zhong Zhu – Department of Physics, Xiamen University, Xiamen 361005, China; orcid.org/0000-0001-5353-4418
Shunqing Wu – Department of Physics, Xiamen University, Xiamen 361005, China; orcid.org/0000-0002-2545-0054

Complete contact information is available at: <https://pubs.acs.org/doi/10.1021/acsami.4c00973>

Notes

The authors declare no competing financial interest.

■ ACKNOWLEDGMENTS

This work is supported by National Natural Science Foundation of China (22073076 and 21933009) and the Fundamental Research Funds for the Central Universities of China (20720210023). Xiamen University High Performance Computing Center is acknowledged for the supercomputer resources. Shaorong Fang and Tianfu Wu from Information and Network Center of Xiamen University are acknowledged for the help with the GPU computing.

■ REFERENCES

- (1) Li, Y.; Xu, L.; Liu, H.; Li, Y. Graphdiyne and graphyne: from theoretical predictions to practical construction. *Chem. Soc. Rev.* **2014**, *43*, 2572–2586.
- (2) Baughman, R. H.; Eckhardt, H.; Kertesz, M. Structure-property predictions for new planar forms of carbon: Layered phases containing sp^2 and sp atoms. *J. Chem. Phys.* **1987**, *87*, 6687–6699.
- (3) Huang, C.; Li, Y.; Wang, N.; Xue, Y.; Zuo, Z.; Liu, H.; Li, Y. Progress in research into 2D graphdiyne-based materials. *Chem. Rev.* **2018**, *118*, 7744–7803.
- (4) Li, G.; Li, Y.; Liu, H.; Guo, Y.; Li, Y.; Zhu, D. Architecture of graphdiyne nanoscale films. *Chem. Commun.* **2010**, *46*, 3256–3258.
- (5) Zheng, X.; Chen, S.; Li, J.; Wu, H.; Zhang, C.; Zhang, D.; Chen, X.; Gao, Y.; He, F.; Hui, L.; Liu, H.; Jiu, T.; Wang, N.; Li, G.; Xu, J.; Xue, Y.; Huang, C.; Chen, C.; Guo, Y.; Lu, T. B.; Wang, D.; Mao, L.; Zhang, J.; Zhang, Y.; Chi, L.; Guo, W.; Bu, X. H.; Zhang, H.; Dai, L.; Zhao, Y.; Li, Y. Two-dimensional carbon graphdiyne: advances in fundamental and application research. *ACS Nano* **2023**, *17*, 14309–14346.
- (6) Li, Q.; Li, Y.; Chen, Y.; Wu, L.; Yang, C.; Cui, X. Synthesis of γ -graphyne by mechanochemistry and its electronic structure. *Carbon* **2018**, *136*, 248–254.
- (7) Desyatkin, V. G.; Martin, W. B.; Aliev, A. E.; Chapman, N. E.; Fonseca, A. F.; Galvao, D. S.; Miller, E. R.; Stone, K. H.; Wang, Z.; Zakhidov, D.; Limpoco, F. T.; Almahdali, S. R.; Parker, S. M.; Baughman, R. H.; Rodionov, V. O. Scalable synthesis and characterization of multilayer gamma-graphyne, new carbon crystals with a small direct band gap. *J. Am. Chem. Soc.* **2022**, *144*, 17999–18008.
- (8) Luo, G.; Qian, X.; Liu, H.; Qin, R.; Zhou, J.; Li, L.; Gao, Z.; Wang, E.; Mei, W.-N.; Lu, J.; Li, Y.; Nagase, S. Quasiparticle energies and excitonic effects of the two-dimensional carbon allotrope graphdiyne: theory and experiment. *Phys. Rev. B* **2011**, *84*, No. 075439.
- (9) Cui, H.-J.; Sheng, X.-L.; Yan, Q.-B.; Zheng, Q.-R.; Su, G. Strain-induced dirac cone-like electronic structures and semiconductor–semimetal transition in graphdiyne. *Phys. Chem. Chem. Phys.* **2013**, *15*, 8179–8185.
- (10) Gao, X.; Liu, H.; Wang, D.; Zhang, J. Graphdiyne: synthesis, properties, and applications. *Chem. Soc. Rev.* **2019**, *48*, 908–936.
- (11) Xi, J.; Wang, D.; Yi, Y.; Shuai, Z. Electron-phonon couplings and carrier mobility in graphynes sheet calculated using the Wannier-interpolation approach. *J. Chem. Phys.* **2014**, *141*, No. 034704.
- (12) Srinivasu, K.; Ghosh, S. K. Graphyne and graphdiyne: promising materials for nanoelectronics and energy storage applications. *J. Phys. Chem. C* **2012**, *116*, 5951–5956.
- (13) Sun, M.; Dougherty, A. W.; Huang, B.; Li, Y.; Yan, C. H. Accelerating atomic catalyst discovery by theoretical calculations-machine learning strategy. *Adv. Energy Mater.* **2020**, *10*, No. 1903949.
- (14) Zhai, X.; Yan, H.; Ge, G.; Yang, J.; Chen, F.; Liu, X.; Yang, D.; Li, L.; Zhang, J. The single-Mo-atom-embedded-graphdiyne monolayer with ultra-low onset potential as high efficient electrocatalyst for N_2 reduction reaction. *Appl. Surf. Sci.* **2020**, *506*, No. 144941.
- (15) He, T.; Zhang, L.; Kour, G.; Du, A. Electrochemical reduction of carbon dioxide on precise number of Fe atoms anchored graphdiyne. *J. CO₂ Util.* **2020**, *37*, 272–277.
- (16) Liu, T.; Wang, Q.; Wang, G.; Bao, X. Electrochemical CO_2 reduction on graphdiyne: a DFT study. *Green Chem.* **2021**, *23*, 1212–1219.
- (17) Liu, X.; Wang, Z.; Tian, Y.; Zhao, J. Graphdiyne-supported single iron atom: a promising electrocatalyst for carbon dioxide electroreduction into methane and ethanol. *J. Phys. Chem. C* **2020**, *124*, 3722–3730.
- (18) Ma, D.; Zeng, Z.; Liu, L.; Jia, Y. Theoretical screening of the transition metal heteronuclear dimer anchored graphdiyne for electrocatalytic nitrogen reduction. *J. Energy Chem.* **2021**, *54*, 501–509.
- (19) Song, W.; Xie, K.; Wang, J.; Guo, Y.; He, C.; Fu, L. Density functional theory study of transition metal single-atoms anchored on graphyne as efficient electrocatalysts for the nitrogen reduction reaction. *Phys. Chem. Chem. Phys.* **2021**, *23*, 10418–10428.
- (20) Song, W.; Fu, L.; He, C.; Xie, K. Carbon-coordinated single Cr site for efficient electrocatalytic N_2 fixation. *Adv. Theory Simul.* **2021**, *4*, No. 2100044.
- (21) Fu, L.; Wang, R.; Zhao, C.; Huo, J.; He, C.; Kim, K.-H.; Zhang, W. Construction of Cr-embedded graphyne electrocatalyst for highly

- selective reduction of CO₂ to CH₄: A DFT study. *Chem. Eng. J.* **2021**, *414*, No. 128857.
- (22) Cao, J.; Li, N.; Zeng, X. Exploring the synergistic effect of B–N doped defective graphdiyne for N₂ fixation. *New J. Chem.* **2021**, *45*, 6327–6335.
- (23) Li, S.; Yam, K.-M.; Guo, N.; Zhao, Y.; Zhang, C. Highly stable two-dimensional metal-carbon monolayer with interpenetrating honeycomb structures. *npj 2D Mater. Appl.* **2021**, *5*, 52.
- (24) Yam, K. M.; Zhang, Y.; Guo, N.; Jiang, Z.; Deng, H.; Zhang, C. Two-dimensional graphitic metal carbides: structure, stability and electronic properties. *Nanotechnology* **2023**, *34*, No. 465706.
- (25) Xiang, Y.; Li, L.; Li, Y.; Zhu, Z.-Z.; Wu, S.; Cao, X. High-density Fe single atoms anchored on 2D-Fe₂C₁₂ monolayer materials for N₂ reduction to NH₃ with high activity and selectivity. *Appl. Surf. Sci.* **2022**, *602*, No. 154380.
- (26) Gui, J.; Li, L.; Yu, B.; Wang, D.; Yang, B.; Gu, Q.; Zhao, Y.; Zhu, Y.; Zhang, Y. Modulation of the coordination environment of copper for stable CO₂ electroreduction with tunable selectivity. *ACS Appl. Mater. Interfaces* **2023**, *15*, 25516–25523.
- (27) Zhang, Y.; Cao, X.; Cao, Z. Unraveling the catalytic performance of the nonprecious metal single-atom-embedded graphitic s-Triazine-based C₃N₄ for CO₂ hydrogenation. *ACS Appl. Mater. Interfaces* **2022**, *14*, 35844–35853.
- (28) Meng, Y.; Cheng, S.-B.; Wu, Z. Atomically dispersed non-noble Cu dimer anchored on a novel graphitic carbon nitride as a promising catalyst for the conversion of CO to CH₂CH₂. *Appl. Surf. Sci.* **2022**, *597*, No. 153761.
- (29) Xiang, Y.; Sun, Y.; Liu, Y.; Liu, Y.; Zhao, J. Computational design of a two-dimensional copper carbide monolayer as a highly efficient catalyst for carbon monoxide electroreduction to ethanol. *ACS Appl. Mater. Interfaces* **2023**, *15*, 13033–13041.
- (30) De Luna, P.; Hahn, C.; Higgins, D.; Jaffer, S. A.; Jaramillo, T. F.; Sargent, E. H. What would it take for renewably powered electrosynthesis to displace petrochemical processes? *Science* **2019**, *364*, 6438.
- (31) Tackett, B. M.; Gomez, E.; Chen, J. G. Net reduction of CO₂ via its thermocatalytic and electrocatalytic transformation reactions in standard and hybrid processes. *Nat. Catal.* **2019**, *2*, 381–386.
- (32) Nielsen, D. U.; Hu, X.-M.; Daasbjerg, K.; Skrydstrup, T. Chemically and electrochemically catalysed conversion of CO₂ to CO with follow-up utilization to value-added chemicals. *Nat. Catal.* **2018**, *1*, 244–254.
- (33) Kresse, G.; Hafner, J. Ab initio molecular dynamics for liquid metals. *Phys. Rev. B* **1993**, *47*, 558–561.
- (34) Kresse, G.; Furthmüller, J. Efficient iterative schemes for ab initio total-energy calculations using a plane-wave basis set. *Phys. Rev. B* **1996**, *54*, 11169–11186.
- (35) Blochl, P. E. Projector augmented-wave method. *Phys. Rev. B* **1994**, *50*, 17953–17979.
- (36) Perdew, J. P.; Burke, K.; Ernzerhof, M. Generalized gradient approximation made simple. *Phys. Rev. L* **1996**, *77*, 3865–3868.
- (37) Grimme, S.; Antony, J.; Ehrlich, S.; Krieg, H. A consistent and accurate ab initio parametrization of density functional dispersion correction (DFT-D) for the 94 elements H–Pu. *J. Chem. Phys.* **2010**, *132*, 19.
- (38) Monkhorst, H. J.; Pack, J. D. Special points for Brillouin-zone integrations. *Phys. Rev. B* **1976**, *13*, 5188–5192.
- (39) Togo, A.; Tanaka, I. First principles phonon calculations in materials science. *Scripta Mater.* **2015**, *108*, 1–5.
- (40) Henkelman, G.; Uberuaga, B. P.; Jónsson, H. A climbing image nudged elastic band method for finding saddle points and minimum energy paths. *J. Chem. Phys.* **2000**, *113*, 9901–9904.
- (41) Sundararaman, R.; Letchworth-Weaver, K.; Schwarz, K. A.; Gunceler, D.; Ozhabes, Y.; Arias, T. A. JDFTx: Software for joint density-functional theory. *SoftwareX* **2017**, *6*, 278–284.
- (42) Kim, D.; Shi, J.; Liu, Y. Substantial impact of charge on electrochemical reactions of two-dimensional materials. *J. Am. Chem. Soc.* **2018**, *140*, 9127–9131.
- (43) Sundararaman, R.; Goddard III, W. A. The charge-asymmetric nonlocally determined local-electric (CANDLE) solvation model. *J. Chem. Phys.* **2015**, *142*, No. 064107.
- (44) Hu, Y.; Jiang, J.; Zhang, P.; Ma, Z.; Guan, F.; Li, D.; Qian, Z.; Zhang, X.; Huang, P. Prediction of Nonlayered Oxide Monolayers as Flexible High-κ Dielectrics with Negative Poisson's Ratios. *Nat. Commun.* **2023**, *14*, 6555.
- (45) He, M.; An, W.; Wang, Y.; Men, Y.; Liu, S. Hybrid metal-boron diatomic site embedded in C₂N monolayer promotes C–C coupling in CO₂ electroreduction. *Small* **2021**, *17*, No. e2104445.
- (46) Liu, H.; Huang, Q.; An, W.; Wang, Y.; Men, Y.; Liu, S. Dual-atom active sites embedded in two-dimensional C₂N for efficient CO₂ electroreduction: A computational study. *J. Energy Chem.* **2021**, *61*, 507–516.
- (47) Xiao, H.; Cheng, T.; Goddard III, W. A. Atomistic mechanisms underlying selectivities in C₁ and C₂ products from electrochemical reduction of CO on Cu(111). *J. Am. Chem. Soc.* **2017**, *139*, 130–136.
- (48) Wang, M.; Xiang, Y.; Chen, W.; Wu, S.; Zhu, Z.-Z.; Cao, X. SiFeN₆-graphene: A promising dual-atom catalyst for enhanced CO₂-to-CH₄ conversion. *Appl. Surf. Sci.* **2024**, *643*, No. 158724.
- (49) Jitwatanasirikul, T.; Roongcharoen, T.; Sikam, P.; Takahashi, K.; Rungrotmongkol, T.; Namuangruk, S. The screening of homo- and hetero-dual atoms anchored graphdiyne for boosting electrochemical CO₂ reduction. *Adv. Mater. Interfaces* **2023**, *10*, No. 2201904.
- (50) Xiao, Y.; Zhang, W. High throughput screening of M₃C₂ MXenes for efficient CO₂ reduction conversion into hydrocarbon fuels. *Nanoscale* **2020**, *12*, 7660.